



High-resolution polarization-sensitive Fourier ptychography microscopy using a high numerical aperture dome illuminator

MAHDIEH GHOLAMI MAYANI,^{1,*} KIM ROBERT TEKSETH,² DAG WERNER BREIBY,^{1,2} JÖRN KLEIN,³ AND MUHAMMAD NADEEM AKRAM¹ 

¹Department of Microsystems, University of South-Eastern Norway (USN), Vestfold Innovation Park, Raveien 205, 3184 Borre, Norway

²PoreLab, Department of Physics, Norwegian University of Science and Technology (NTNU), Høgskoleringen 5, 7491 Trondheim, Norway

³Department of Nursing and Health Sciences, University of South-Eastern Norway (USN), Campus Porsgrunn, Norway

*mghol@usn.no

Abstract: Polarization-sensitive Fourier-ptychography microscopy (pFPM) allows for high resolution imaging while maintaining a large field of view, and without mechanical movements of optical-setup components. In contrast to ordinary light microscopes, pFPM provides quantitative absorption and phase information, for complex and birefringent specimens, with high resolution across a wide field of view. Using a semi-spherical home-built LED illumination array, a single polarizer, and a 10x /0.28NA objective, we experimentally demonstrate high performance pFPM with a synthesized NA of 1.1. Applying the standard quantitative method, a measured half-pitch resolution of 244 nm is achieved for the 1951 USAF resolution test target. As application examples, the polarimetric properties of a herbaceous flowering plant and the metastatic carcinoma of human liver cells are analyzed and quantitatively imaged.

© 2022 Optica Publishing Group under the terms of the [Optica Open Access Publishing Agreement](#)

1. Introduction

Polarization imaging methods, providing information on cellular structures, are beneficial in the pathology and biology laboratories [1–5]. Observing the polarization-sensitive fringe pattern is a challenging task in ordinary light microscopes. In [6], several methods have been discussed for polarization information extraction in microscopic imaging such as using polarizing films for circular dichroism, or strain birefringence measurements where the sample is positioned between two polarizing plates and differential-interference contrast is visualized. By using a vector-based representation of the polarization state, the effect of polarizers or retarders can be quantitatively represented by matrices. Mueller calculus and Jones calculus are the most commonly used matrix formalisms, for the partially coherent and fully coherent propagation of light, respectively [7].

Polarimetric analysis is useful for defect tracing in crystalline semiconductor components [8,9], and for clinical pathology diagnosis [10,11] such as early-stage cancer detection [12] in which the polarization technique allows to visualize the collagen and parasites changes without the need for special preparations of the samples. When extracting birefringence maps of anisotropic specimens, a high resolution (HR) and a large field of view (FoV) are desired. Polarimetric imaging with simultaneous HR and wide FOV in conventional microscopes is not yet feasible. Although multiple sub-images can be stitched together to create a wide FOV, this is a labor-intensive and time-consuming process [13].

Alleviating these challenges, Fourier ptychography microscopy (FPM) is a powerful imaging technique, achieving a HR recovered image while maintaining a large FOV by using a low

magnification objective [14]. In FPM, a light-emitting diode (LED) array provides angularly-varying coherent illumination on the sample which leads to a shift in the object's spatial frequency spectrum in the Fourier plane [15]. A digital camera records a series of images corresponding to the central and off-axis LEDs. This method can be used in combination with polarization-sensitive microscopy, here referred to as pFPM, where the incident light on the sample is fully polarized and the employed digital camera is equipped with a polarization sensor [16,17]. Recently, researchers have developed an interest in pFPM [16,17]. In their setups, planar LED boards with the size of 15×15 LEDs were used, providing illumination NA (NA_{illum}) of 0.41. Compared to the planar LED boards, dome-shaped LED arrays provide higher NA_{illum} and better signal-to-noise ratio (SNR), especially for dark-field images. Because of the lower power falloff as a function of incidence angle with the dome structure [18], an intensity falloff of $\sim \cos \theta$ is achieved whereas the planar LED array gives an intensity drop $\sim \cos^4 \theta$ [19]. Furthermore, the dome geometry allows for higher NA_{illum} with fewer LEDs, contributing to faster capturing and post-processing. In conventional FPMs, dome- [18,19] and quasi-dome shaped LED [20,21] configurations have been used. However, dome-based polarimetric studies have not been reported yet.

In this work, we have developed a dome LED array that integrates into the pFPM setup yielding $NA_{illum} = 0.82$, which is approximately twice what is practically achievable with a planar LED board. We also used 217 LEDs, fewer than in previous studies [16,17]. This paper is organized as follows: Using Jones vector calculation, described in Section 2, the basic mathematical theory related to pFPM is outlined. Section 3 is devoted to the experimental implementation and we verify the spatial resolution along with phase delay and phase retardation for a high resolution USAF's test target. It is followed by analysis of a herbaceous flowering plant sample and a human liver tissue for interpretation of liver fibrosis stage, for the assessment of pFPM's performance. Finally, the conclusion and future research plans are discussed.

2. Mathematical description of pFPM

This section is devoted to the mathematical description of pFPM wherein Jones calculus is used to quantitatively evaluate the polarization dependency of the reconstructed high resolution image. A schematic of the pFPM optical setup is shown in Fig. 1. A home-built dome-shaped LED array controlled by a programmed Arduino board is used to illuminate the sample. Assuming that each LED is quasi-monochromatic and spatially coherent, the electric field plane wave emitted by the n^{th} LED within the array, can be described by $\mathbf{E}_{in} = \mathbf{E}_0 \exp(i \mathbf{k}_n \cdot \mathbf{r})$ in which $|\mathbf{k}_n| = 2\pi/\lambda$ and λ is the operating wavelength. By utilizing a left-handed circular polarizer (LHCP), a uniform un-polarized plane wave is transformed into a circularly-polarized wave that falls on the sample plane. If the electric field in terms of amplitude and phase of the x and y components are given as $E_{0x} \exp(i\phi_x)$ and $E_{0y} \exp(i\phi_y)$ with $E_{0x} = E_{0y}$ and a corresponding phase lag of $\phi_x = \phi_y - \pi/2$, the normalized Jones vector of the left circularly-polarized light can be written in the form of $\mathbf{J}_{lcp} = (1/\sqrt{2})[1; i]$. The polarized wave goes through the thin specimen with unknown electromagnetic properties, whereby the polarization is changed from circular to elliptical to various degrees in each region of the sample. Anisotropic materials such as certain crystals like calcite, and biological tissues, have varying refractive indices, corresponding to different phase velocities in relation to the molecular orientation. As presented in Fig. 2, two orthogonal eigen polarizations e_1 and e_2 are associated with the electric field vector \mathbf{E} in which the polarization is defined under the elliptical angle χ and slope angle θ .

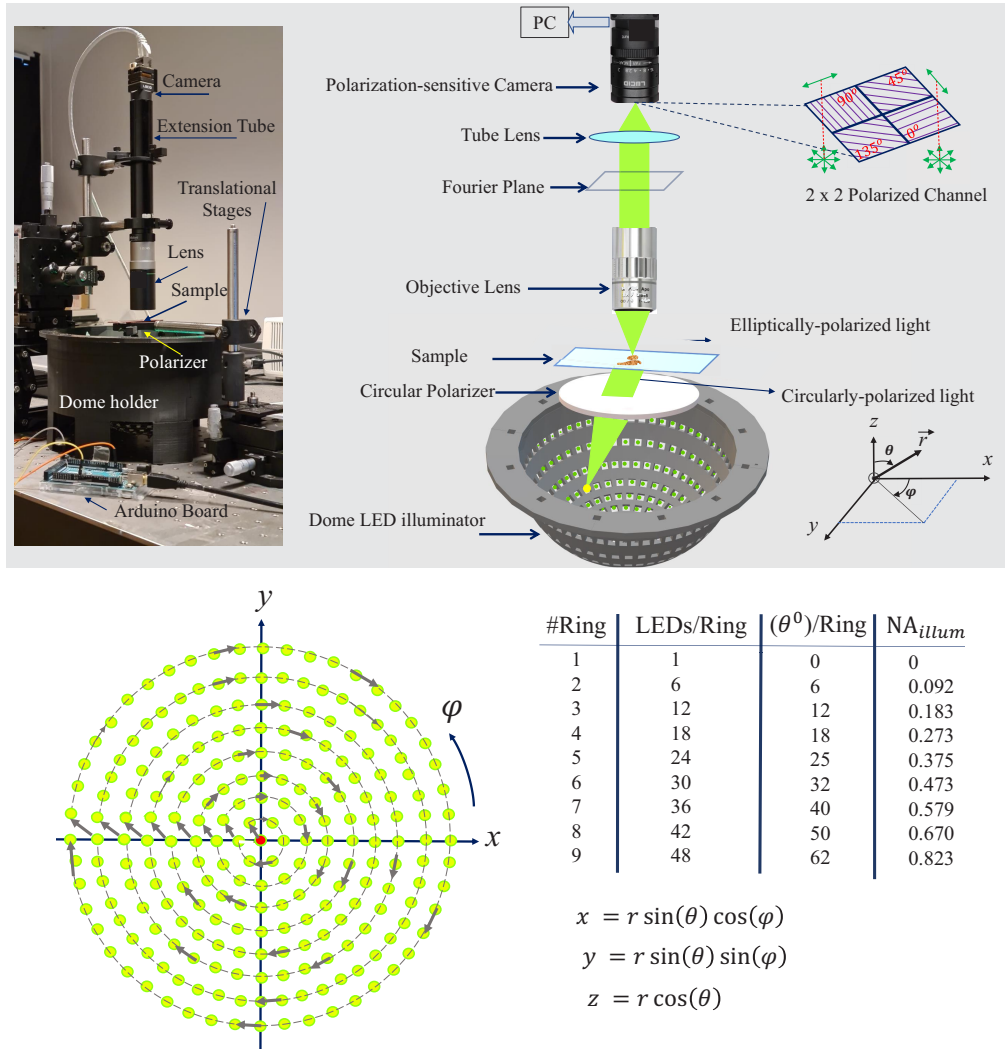


Fig. 1. Schematic of the pFPM setup. Circularly-polarized light passes through the sample and the polarization-sensitive camera captures images in four polarization angles 0°, 45°, 90°, 135°. The LED illumination sequences and LED positions along with their NA_{illum} are presented in the table.

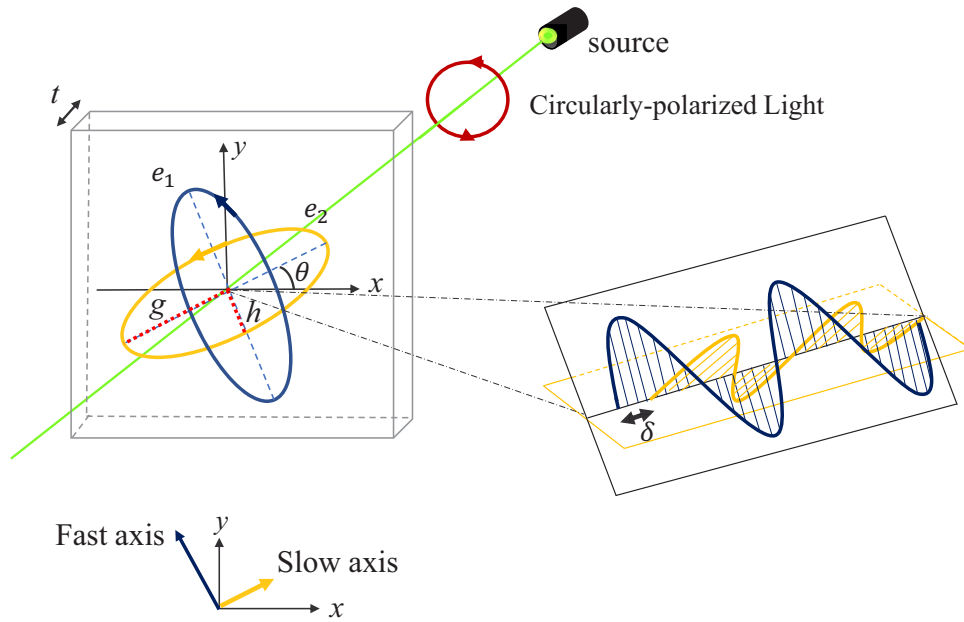


Fig. 2. Circularly-polarized light incident on an anisotropic sample and elliptical polarization coinciding planes are shown with the fast and slow axes. The light travels with different phase velocities, for a general birefringent sample. Two orthogonal Eigen polarizations e_1 and e_2 are associated with the electric field vector \mathbf{E} in which the polarization is defined under the elliptical angle χ and slope angle θ .

Generally, the Jones matrix of an anisotropic medium without gain and dissipation is described as [22]:

$$\mathbf{M}(\delta, \theta, \chi) = \begin{pmatrix} \cos \frac{\delta}{2} - i \sin \frac{\delta}{2} \cos 2\theta \cos 2\chi & -i \sin \frac{\delta}{2} (\sin 2\theta \cos 2\chi - i \sin 2\chi) \\ -i \sin \frac{\delta}{2} (\sin 2\theta \cos 2\chi + i \sin 2\chi) & \cos \frac{\delta}{2} + i \sin \frac{\delta}{2} \cos 2\theta \cos 2\chi \end{pmatrix} \quad (1)$$

where δ and θ respectively correspond to the phase retardation (in radians) and optic-axis orientation. For linear birefringence, the elliptical angle $\chi = \arctan(g/h)$ is zero when the ratio of the ellipse semi-axes g and h approaches 0, and $\chi = \pi/4$ in the case of circular birefringence characteristics.

The wave transmitted through the specimen is collected by a 10x /0.28NA infinity-conjugate objective lens and a tube lens to focus the light on the digital camera. The optical system with a limited optical cutoff frequency is simulated using a coherent transfer function (CTF), with a circular pupil $P(k_x, k_y)$ in the frequency domain, behaving as a low-pass filter. The light is scattered by the sample into the objective containing the optical aperture stop of the system. Fourier ptychography method goes beyond the diffraction limit by spectrum shifting when applying off-axis illumination angles. Here, the angular-varying illumination is carried out using a dome-shaped LED array with LEDs arranged at specified angles and positions, as illustrated in Fig. 1.

The image recording is provided by a CMOS camera equipped with a polarization-sensitive sensor. The camera sensor array is grouped in blocks of 2×2 pixels, with each pixel sporting a linear polarization filter of orientation $\phi \in [0^\circ, 45^\circ, 90^\circ, 135^\circ]$, having associated Jones matrix of $\mathbf{L}_\phi = (\cos^2 \phi \quad \sin \phi \cos \phi; \sin \phi \cos \phi \quad \sin^2 \phi)$ [16]. The intensity of light passing through the

LHCP, complex sample and camera sensor contains the necessary information for reconstructing the polarization properties of the sample [23]. For each polarization state ϕ subject to the n^{th} illumination angle, the pixel-by-pixel electric field on the camera sensor can be described as:

$$\mathbf{E}_{\phi}^n = \mathbf{L}_{\phi} \mathbf{M} \mathbf{J}_{lcp} \mathbf{E}_{in} \quad (2)$$

and the imaged intensity is subsequently defined as $\mathbf{I}_{\phi}^n = |\mathbf{E}_{\phi}^n|^2$. The full-polarized image overlaid from the camera sensor involves four polarized neighboring pixels. Therefore, to project the raw image onto four separate polarization channels, a demosaicing technique is utilized. This procedure is outlined in Fig. 3. The missing information between pixels is estimated through bicubic interpolation, applied separately to each polarization orientation [24]. A pFPM recovery, including the phase, is required to reconstruct a high resolution complex image from the low resolution (LR) interpolated images. The process involves shifting the frequency within the Fourier space, thereby extending the object spatial spectrum. Several iterations are needed to accomplish a faithful recovery. This scheme is carried out by propagating the field to the image plane where the the field amplitude is replaced by the square root of the LR captured intensities. The field is then propagated back to the Fourier plane to substitute the appropriate sub-spectrum. This cycle is repeated until the convergence error is minimized [25]. Additionally, pFPM efficiently compensates any optical aberrations, such as defocus, by estimating and digitally correcting the unknown pupil aberration of the utilized objective lens. Thus, each of the digitally-refocused segments of the entire image are stitched together to reconstruct the HR complex image for each polarization channel.

To avoid sampling artifacts and aliasing, the Nyquist criterion has to be satisfied. Therefore, the maximum frequency of the calculated spectrum must be less than $1/(2 \delta r_x)$ where the spatial resolution is selected to be δr_x in pFPM.

The LEDs are deployed densely in the center of the dome and get more sparsely towards the outer edge, to maintain a sufficient spectrum overlap between adjacent illuminated LEDs and having a better convergence rate for the image recovery. In addition, this scheme leads to less recovery artifacts. To effectively increase the speed and accuracy of the recovery, it is important that the object spectrum overlap between adjacent rings exceeds 50% [26]. As opposed to the planar LED geometry, the dome facilitates keeping a constant spectrum overlap, resulting in a minimum number of required LEDs to achieve a certain NA_{synth} .

It is worth mentioning that to increase the spectrum overlap in the planar LED board configuration, larger incident angles are necessary, thus requiring a greater number of LEDs. In addition, larger illumination angle with a planar LED array further reduces the light intensity falling on the sample, resulting in a poor signal-to-noise ratio that adversely affects the recovery of pFPM. The total number of LEDs, used by the designed dome, as well as the sequence of the LED illumination and position coordinates, are presented in Fig. 1.

To quantitatively recover the polarimetric sample properties, the retardation and optic axis orientation can be extracted from the measured intensities [27]. By using Eq. (2), the intensity matrix of a linear birefringence can be written as:

$$\mathbf{I}_{\phi} = \mathbf{I}_b + \mathbf{I}_a(1 - \sin \delta \sin 2(\phi - \theta))/2 \quad (3)$$

in which \mathbf{I}_b can be explicitly added to the intensity expression [28], representing stray light or background illumination. According to Eq. (3), there are four unknowns I_a , I_b , δ , and θ . Therefore, just four independent measurements, as provided by the four polarization channels in this study (0° , 45° , 90° , 135°), are sufficient to assess these parameters. However, to more accurately extract the Jones polarization parameters, it has been suggested to use at least six optical channel arrangements [29]. The intensity distributions for the four polarization channels

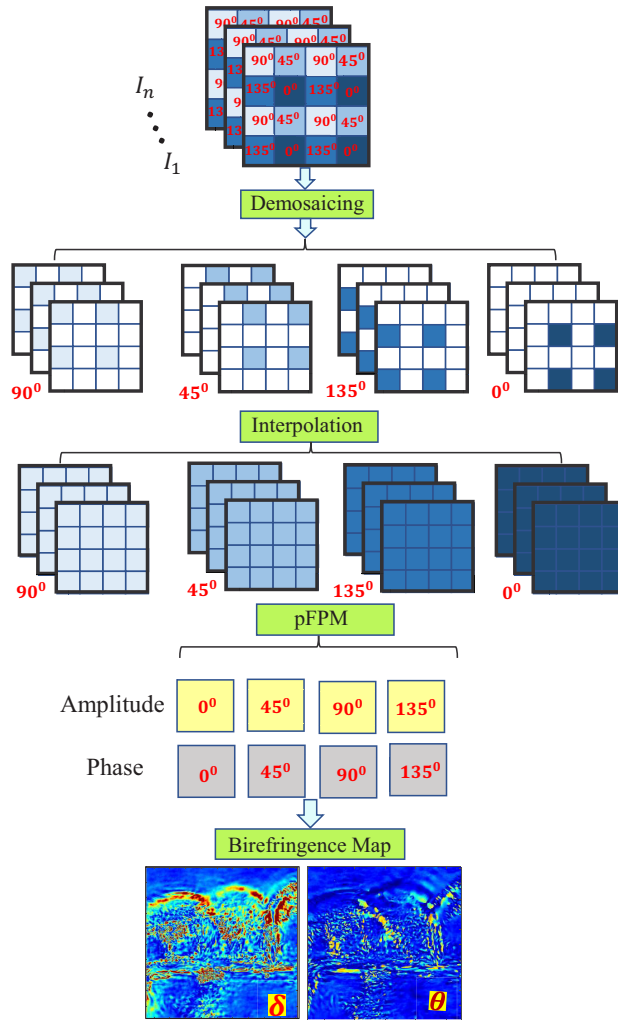


Fig. 3. Image decomposition technique to reconstruct the images corresponding to each of the four polarization orientations and the polarimetric birefringence map (δ and θ) by pFPM.

simplify as follows:

$$\begin{aligned}
 \mathbf{I}_1 &= \mathbf{I}_0 - \mathbf{I}_b = \mathbf{I}_a(1 + \sin \delta \sin 2\theta)/2 \\
 \mathbf{I}_2 &= \mathbf{I}_{45} - \mathbf{I}_b = \mathbf{I}_a(1 - \sin \delta \cos 2\theta)/2 \\
 \mathbf{I}_3 &= \mathbf{I}_{90} - \mathbf{I}_b = \mathbf{I}_a(1 - \sin \delta \sin 2\theta)/2 \\
 \mathbf{I}_4 &= \mathbf{I}_{135} - \mathbf{I}_b = \mathbf{I}_a(1 + \sin \delta \cos 2\theta)/2
 \end{aligned} \tag{4}$$

After subtracting the I_b from each image and some mathematical simplifications, the phase retardation δ (≥ 0) and optic axis orientation θ ($0 \leq \theta \leq \pi$) can be derived as [16]:

$$\begin{aligned}
 \delta &= \sin^{-1} \sqrt{\left(\frac{\mathbf{I}_1 - \mathbf{I}_3}{\mathbf{I}_1 + \mathbf{I}_3}\right)^2 + \left(\frac{\mathbf{I}_4 - \mathbf{I}_2}{\mathbf{I}_4 + \mathbf{I}_2}\right)^2} \\
 \theta &= \frac{1}{2} \tan^{-1} \left(\frac{\mathbf{I}_1 - \mathbf{I}_3}{\mathbf{I}_4 - \mathbf{I}_2}\right)
 \end{aligned} \tag{5}$$

(Please note that if we follow the notation of the \mathbf{P} matrix in Song's paper [16], there is a sign error in his \mathbf{J}_s matrix. Please refer to the Appendix for more details).

3. pFPM experimental implementation, results and discussion

In this section, pFPM based on a high $NA_{synth} = 1.1$ is experimentally demonstrated. In order to validate its performance, first, a USAF 1951 test target (from *Ready Optics*), exhibiting a standard resolution chart, was investigated; followed by a polarimetric analysis of anisotropic herbaceous flowering plant sample and human liver cancer tissue (both provided by Johannes Lieder GmbH).

The light coming from the LED array is polarized using a zero-order left-handed circular polarizer (provided by Edmund Optics, CP42HE). The zero-order reduces the complications associated with light at an oblique incidence through the polarizer. The circular polarization is transformed into the elliptical polarization state after passing through the sample. We have used a polarization sensitive camera to collect images through a 10x /0.28NA objective lens. The CMOS camera (from LUCID vision lab, PHX050S, 2448 × 2048 pixels count and 3.45 μm pixel size) utilizes a polarization-sensitive front sensor to simultaneously capture images in four different polarization channels, i.e., 0°, 45°, 90°, 135°; thereby eliminating the need to rotate polarizers and/or variable retarders. There are no mechanical movements needed with our setup. The dome LED array with a radius of 120 mm was positioned with its spherical center 16.6 mm below the sample plane. There are 9 rings having 217 LEDs with the operation wavelength $\lambda = 525 \pm 20$ nm in the dome used.

The sample was sequentially illuminated from various angles by LEDs to achieve a maximum $NA_{illum} = 0.82$. With the demosaicing approach, raw images were separated into their respective polarization states, and then a standard interpolation method was employed to fill in missing data in empty pixels [24].

In the polarized CMOS camera, the Nyquist sampling requirement is: pixel size of LR image of each channel $\leq \lambda/4/NA_{obj}$. This requirement is satisfied in our case (0.345 μm pixel size on the object plane vs 0.473 μm Nyquist requirement). For the HR recovered object, the Nyquist requirement is: pixel size of HR image $\leq \lambda/4/NA_{synth}$. This requirement is also satisfied as we choose pixel size of HR to be 0.08625 μm (4 times upscaling of LR image) while the Nyquist requirement is 0.12 μm .

In order to have a sufficient signal-to noise-ratio, especially for dark-field images, the intensity levels within the captured images have been adjusted by the output histogram's shape [30]. An optimum brightness and contrast in the objective image was achieved by adjusting the gain and exposure time of the recording system based on the output of the histogram [31]; thereby avoiding underexposed or overexposed captured images. The embedded pupil recovery (EPRY) algorithm was applied to the phase retrieval iteration technique in order to improve the convergence and achieve aberration correction [32]. In addition, the iteration loops, applied to the experimental

data set of each channel, continued until convergence was reached and HR complex images for all four polarization orientations were successfully recovered [25].

3.1. Highly-resolved pFPM image of the USAF amplitude target

All the images of the USAF's test target were captured with an exposure time of 400 ms and a camera gain of 15 dB. HR images were obtained by selecting a region of interest from the LR matrix of size 128 pixels by 128 pixels for each polarization channel and an upscaling ratio of 4. By the van Cittert–Zernike theorem, the small patch ensures that the imaging can be considered fully coherent. The performance of our pFPM imaging is shown in Fig. 4, for one channel only at $\phi = 45^\circ$; the results of the other polarization channels are roughly the same. The cut-off frequency of pFPM is slightly above the element 1 of group 11. It is clearly shown that the resolved resolution of 244 nm was successfully obtained, which closely matches the theoretical half-pitch resolution of $\lambda/(2 \text{NA}_{\text{synth}}) = 238$ nm. Because the USAF target is deposited on an isotropic glass substrate, the phase retardation and optic axis orientation values are close to zero. Some non-zero values on the metal surface may be attributed to the structural stressed property and/or inevitable numerical noise. This sample was used as standard metrology, estimating the resolving capability of our pFPM setup under the achieved NA_{synth} . Note that the USAF bars are opaque, and hence the phase and other quantities at these locations may be inaccurate. To clarify the advantages of the utilized dome LED illuminator, there have been provided a comparison between the current work and previous studies in Table 1.

Some noise sources such as cross-polarization from camera filter, inter-channel correlation and dead pixels of the camera are inevitable. The camera being out of focus because of small movements between the camera and object can also distort the image. To improve the reconstruction quality of the algorithm, wavelet-based noise removing techniques were applied to the captured images [33,34].

Table 1. Comparison between the current work and previous studies.

Ref	Number of LEDs	NA_{synth}	Half-pitch resolution	polarization study
[16]	225	0.51	550 nm	Yes
[17]	225	0.51	620 nm	Yes
[18]	415	1.05	244 nm	No
[19]	508	0.87	a few microns	No
Current work	217	1.11	244 nm	Yes

3.2. pFPM performance demonstrated on herbaceous flowering plant sample

In this section, the pFPM study of a prepared microscope slide from *Lilium* flower (through pistil and stigma with pollen and pollen tubes) is presented in Fig. 5, which displays the achieved HR microscopy image and birefringence properties. The quantitative birefringence map illustrates cellular development. To visualize phase retardation and optic axis orientation clearly, a subregion patch has been selected. The recovered results show the close-up of the intracellular spaces of parenchymal cells in the gynoecium.

3.3. Liver fibrosis stage determination by pFPM

Liver fibrosis is clinically silent, but early diagnosis is essential in order to provide the patient with specific therapy and thus prevent progression to liver cirrhosis. Determining the fibrosis stage in patients with chronic liver diseases is of a high clinical relevance since it can guide further diagnostic and therapeutic steps and estimate the patient's prognosis.

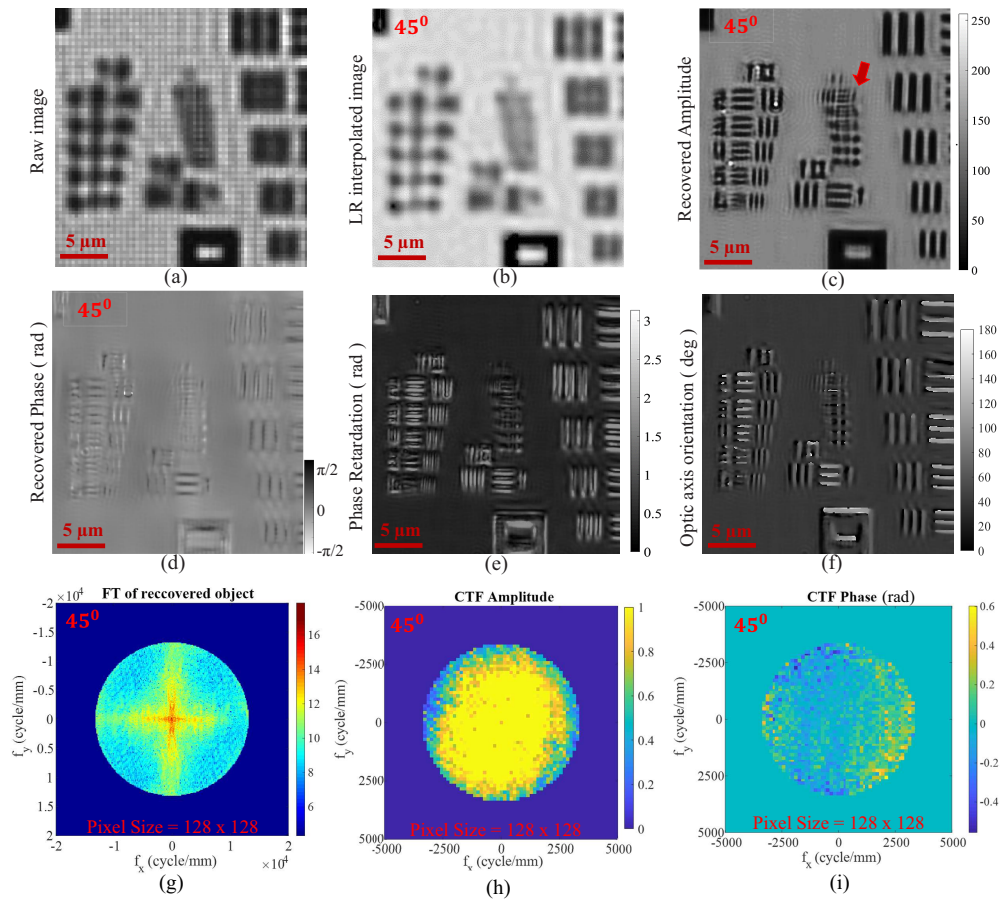


Fig. 4. pFPM recovery of USAF amplitude target. The recovered images shown correspond to $\phi = 45^\circ$. (a) Raw image including four polarization channel information, (b) interpolated low-resolution image, (c) pFPM recovered amplitude, (d) pFPM recovered phase, (e) phase retardation (δ), (f) optic axis rotation (θ), (g) Fourier transform of the recovered object, (h) magnitude of the coherent transfer function (CTF), (i) phase of the CTF. The red arrow in (c) denotes the finest resolved group.

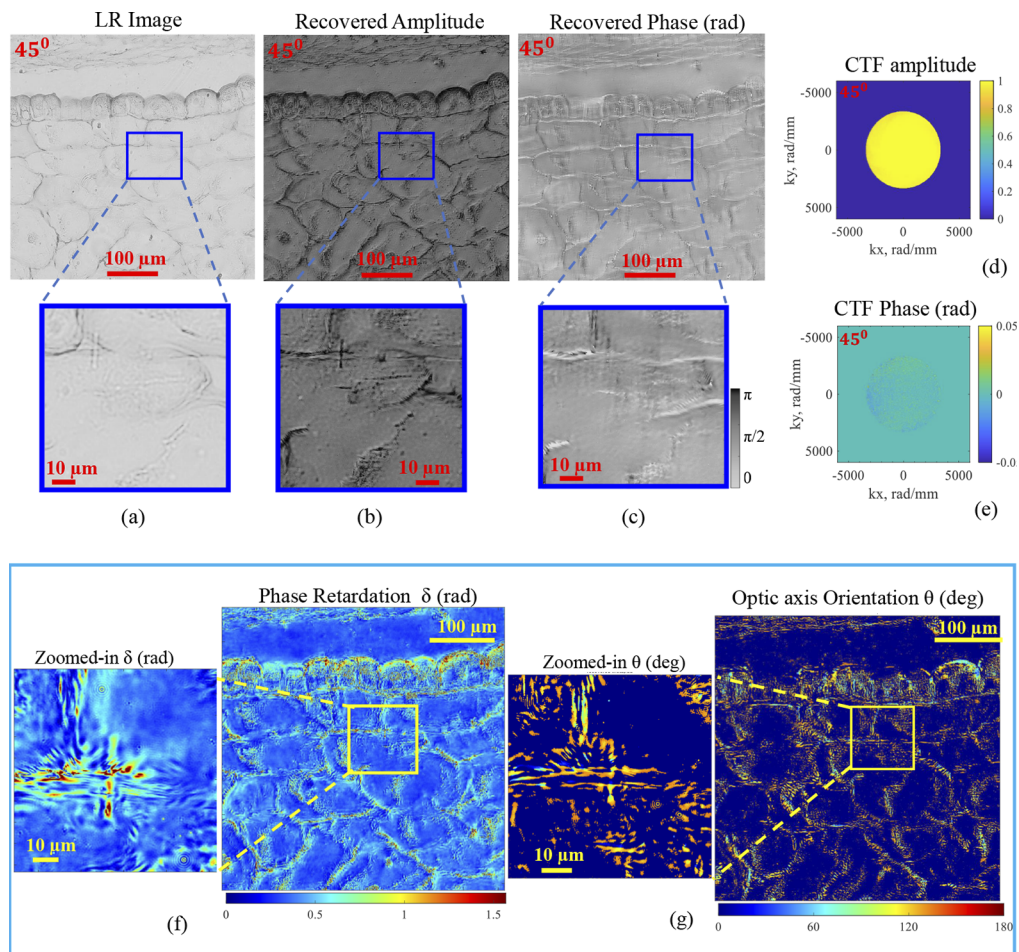


Fig. 5. pFPM performance demonstrated on flowering plant sample and resolved details. (a) Low resolution interpolated image, (b) pFPM recovered amplitude, (c) pFPM recovered phase, (d) amplitude of CTF, (e) phase of CTF, (f) phase retardation (δ) and (g) optic axis orientation (θ). Note that where δ approaches zero, the optic axis orientation θ is undefined.

A semi-quantitative numerical scoring method is commonly used in the clinic to determine the stage of liver fibrosis. This method requires both experienced and well-trained technicians who can stain liver tissue well [12]. pFPM potentially facilitates diagnosis by removing these staining requirements. Figure 6 shows a close-up of the dysplastic focus in the environment of an already established malignant tumor. The closed-up square shows a cell with an abnormal number of chromosomes arranged in a disorganized fashion.

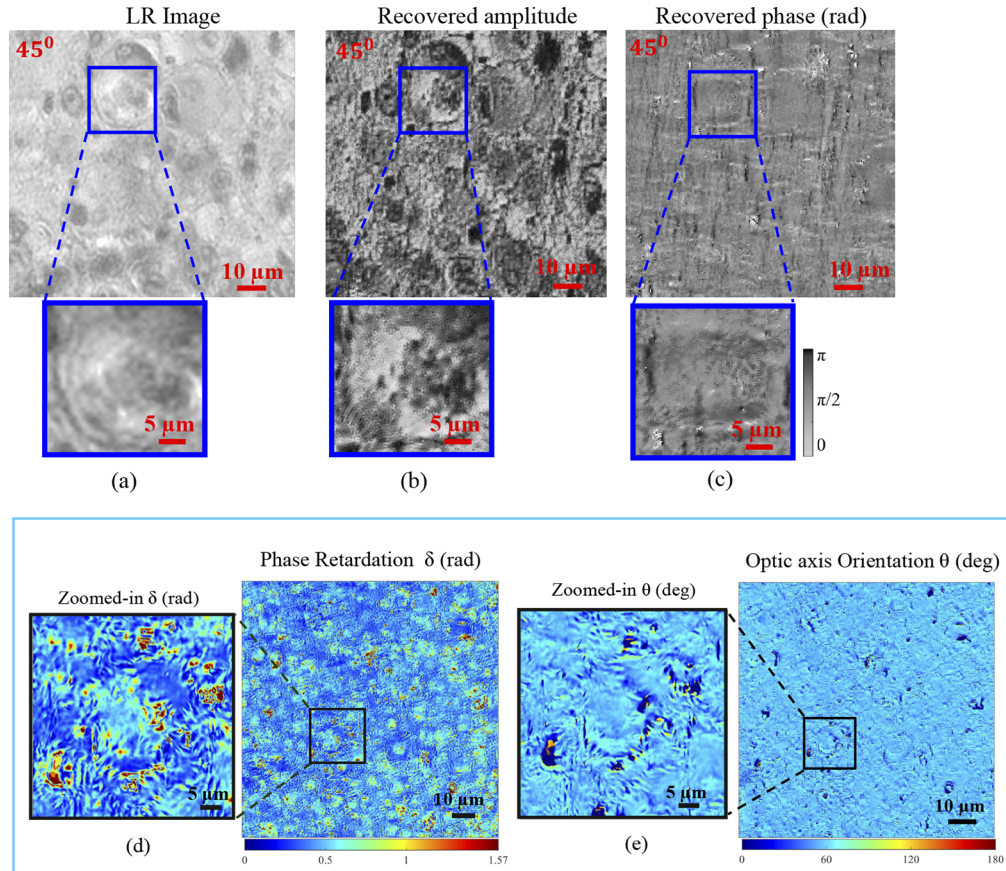


Fig. 6. pFPM performance; determination of liver fibrosis stage: (a) low resolution interpolated image, (b) pFPM recovered amplitude, (c) pFPM recovered phase, (d) phase retardation (δ), (e) optic axis rotation (θ).

4. Conclusion and future works

Through polarization-sensitive high-NA Fourier ptychography and Jones matrix calculation, we have presented highly-resolved quantitative birefringence patterns of complex samples, where no mechanical motion of the optical setup is involved. As opposed to the previous pFPM that used a planar LED board, this work has utilized a home-built dome-shaped LED illuminator with a comparatively low number of LEDs. The hemispherical geometry of the dome contributes to the achievement of the half-pitch resolution of 244 nm and NA_{synth} of 1.1 in a large FOV and maintains sufficient SNR for off-axis LEDs. It is worth mentioning that by decreasing the number of used necessary LEDs, the computational time as well as capturing times decrease. This issue is more pronounced in the case of polarization studies in which four different datasets, corresponding to

different polarization states, should be measured and reconstructed. A flowering plant sample and human liver cancer tissue have been investigated. Using polarization imaging-based quantitative diagnostic methods, multiple staining processes can be reduced, which provides quantitative information to facilitate the adequate staging of liver fibrosis. Due to the sufficient SNR in the dark field images, this setup could be utilized for multilayer thick samples and 3D pFPM as a future work. Furthermore, more step-phase shifting techniques (more than four steps) can be implemented to evaluate polarimetric parameters with higher accuracy in the birefringence mapping approach [29], considered as a future research topic.

Appendix

\mathbf{P} represents a phase shift between orthogonal electric field components along with x and y axes. One may split this phase shift into a phase advance of $\delta/2$ assigned to the fast axis and a phase retardation of $-\delta/2$ corresponding to the slow axis. Therefore, \mathbf{P} with the wave propagator ($kz - \omega t$) can be expressed as $\mathbf{P} = \begin{pmatrix} e^{-i\delta/2} & 0 \\ 0 & e^{+i\delta/2} \end{pmatrix}$. Using this matrix, the Jones matrix of the thin specimen and Eqs. (3)–5 can be obtained.

To evaluate birefringence from intensities according to Eq. (5), two auxiliary variables were defined [16]:

$$\mathbf{V}_1 = \begin{pmatrix} \mathbf{I}_1 - \mathbf{I}_3 \\ \mathbf{I}_1 + \mathbf{I}_3 \end{pmatrix}, \quad \mathbf{V}_2 = \begin{pmatrix} \mathbf{I}_4 - \mathbf{I}_2 \\ \mathbf{I}_4 + \mathbf{I}_2 \end{pmatrix}. \quad (6)$$

The four-quadrant inverse tangent $\arctan2(\mathbf{V}_1, \mathbf{V}_2)$ yields $-\pi \leq 2\theta \leq \pi$. Physically, θ should be in the range of $[0, \pi]$. Therefore, optic axis orientation can be calculated as follows:

$$\begin{aligned} \Theta &= \arctan2(\mathbf{V}_1, \mathbf{V}_2) \\ \text{if } \Theta < 0, \quad \Theta &= \Theta + 360; \text{ end} \\ \text{Finally } \theta &= \Theta/2. \end{aligned} \quad (7)$$

Funding. Research Council of Norway through FRINATEK (275182); NANO2021 (272248); PhD scholarship (2700114).

Disclosures. The authors declare no conflicts of interest.

Data availability. Data supporting the findings of this study are available from the corresponding author, Mahdieh Gholami Mayani, upon reasonable request.

References

1. Y. Zhu, G. Yang, S. Li, L. Wang, X. Jin, Y. Liang, W. Zhao, and H. Li, "Quantitative polarization imaging of zebrafish muscle structures," *Acta Opt. Sin.* **39**(8), 0811001 (2019).
2. R. Strack, "Polarized structured illumination microscopy," *Nat. Methods* **16**(12), 1206 (2019).
3. O. Wagner, M. Schultz, E. Edri, R. Meir, E. Barnoy, A. Meiri, H. Shpaisman, E. Sloutskin, and Z. Zalevsky, "Imaging of nanoparticle dynamics in live and apoptotic cells using temporally-modulated polarization," *Sci. Rep.* **9**(1), 1650 (2019).
4. J. E. Park, Z. Xin, D. Y. Kwon, S. W. Kim, H. Lee, M. J. Jung, S. Tang, T. Y. Ko, J. H. Choi, J. H. Kim, Y. C. Ahn, and C. Oak, "Application of polarization sensitive-optical coherence tomography to the assessment of phase retardation in subpleural cancer in rabbits," *Tissue Eng. Regen. Med.* **18**(1), 61–69 (2021).
5. O. Sijilmassi, J. M. López-Alonso, A. Del Río Sevilla, and M. del Carmen Barrio Asensio, "Development of a polarization imaging method to detect paraffin-embedded pathology tissues before applying other techniques," *J. Biophotonics* **14**(1), e202000288 (2021).
6. M. Bass, C. Decusatis, and J. Enoch, *Handbook of Optics : Geometrical and Physical Optics, Polarized Light, Components and Instruments*, vol. I (OSA, Optical society of America, 2013), 3rd ed.
7. R. A. Chipman, W.-S. T. Lam, and G. Young, "Polarized light and optical systems," *Polarized Light and Optical Systems I* (2018).
8. B. H. Lee, S.-B. Chin, D. H. Cho, C.-L. Song, J.-H. Yeo, D. Some, and S. Reinhorn, "Optical characterization of defects on patterned wafers: exploring light polarization," in *Metrology, Inspection, and Process Control for Microlithography XVIII*, vol. 5375 R. M. Silver, ed., International Society for Optics and Photonics (SPIE, 2004), pp. 849–858.

9. K. Wang, L. Jing, Q. Yao, J. Zhang, X. Cheng, Y. Yuan, C. Shang, J. Ding, T. Zhou, H. Sun, W. Zhang, and H. Li, "Highly in-plane polarization-sensitive photodetection in cspbbr_3 single crystal," *J. Phys. Chem. Lett.* **12**(7), 1904–1910 (2021).
10. S. Cho, S. Kim, Y. Kim, and Y. K. Park, "Optical imaging techniques for the study of malaria," *Trends Biotechnol.* **30**(2), 71–79 (2012).
11. M. Sobczak, M. Asejczyk, K. Kalinowski, and B. Pierscionek, "Comparative analysis of the corneal birefringence pattern in healthy children and adults," *Ophthalmic Physiol. Opt.* **41**(4), 715–725 (2021).
12. Y. Wang, H. He, J. Chang, C. He, S. Liu, M. Li, N. Zeng, J. Wu, and H. Ma, "Mueller matrix microscope: a quantitative tool to facilitate detections and fibrosis scorings of liver cirrhosis and cancer tissues," *J. Biomed. Opt.* **21**(7), 071112 (2016).
13. N. J. Jan, K. Lathrop, and I. A. Sigal, "Collagen Architecture of the Posterior Pole: High-Resolution Wide Field of View Visualization and Analysis Using Polarized Light Microscopy," *Invest. Ophthalmol. Visual Sci.* **58**(2), 735–744 (2017).
14. G. Zheng, R. Horstmeyer, and C. Yang, "Wide-field, high-resolution Fourier ptychographic microscopy," *Nat. Photonics* **7**(9), 739–745 (2013).
15. J. W. Goodman, *Introduction to Fourier optics* (W.H. Freeman Macmillan Learning, 2017), 4 edition. ed.
16. S. Song, J. Kim, S. Hur, J. Song, and C. Joo, "Large-area, high-resolution birefringence imaging with polarization-sensitive fourier ptychographic microscopy," *ACS Photonics* **8**(1), 158–165 (2021).
17. X. Dai, S. Xu, X. Yang, K. C. Zhou, C. Glass, P. C. Konda, and R. Horstmeyer, "Quantitative jones matrix imaging using vectorial fourier ptychography," *Biomed. Opt. Express* **13**(3), 1457–1470 (2022).
18. A. Pan, Y. Zhang, K. Wen, M. Zhou, J. Min, M. Lei, and B. Yao, "Subwavelength resolution fourier ptychography with hemispherical digital condensers," *Opt. Express* **26**(18), 23119–23131 (2018).
19. Z. F. Phillips, M. V. D'Ambrosio, L. Tian, J. J. Rulison, H. S. Patel, N. Sadras, A. V. Gande, N. A. Switz, D. A. Fletcher, and L. Waller, "Multi-contrast imaging and digital refocusing on a mobile microscope with a domed led array," *PLoS One* **10**(5), e0124938 (2015).
20. Z. F. Phillips, R. Eckert, and L. Waller, "Quasi-dome: A self-calibrated high-na led illuminator for fourier ptychography," in *Imaging and Applied Optics 2017*, (Optical Society of America, 2017), p. IW4E.5.
21. R. Eckert, Z. F. Phillips, and L. Waller, "Efficient illumination angle self-calibration in fourier ptychography," *Appl. Opt.* **57**(19), 5434–5442 (2018).
22. E. A. Mironov, "Description of the birefringence effect in optical media with several types of anisotropy," *IEEE J. Quantum Electron.* **57**(5), 1–7 (2021).
23. D. H. Goldstein, *Polarized light* (CRC Press, 2011), 3rd ed.
24. R. Keys, "Cubic convolution interpolation for digital image processing," *IEEE Trans. Acoust., Speech, Signal Process.* **29**(6), 1153–1160 (1981).
25. G. Zheng, *Fourier Ptychographic Imaging*, 2053–2571 (Morgan and Claypool Publishers, 2016).
26. Q. Liu, C. Kuang, Y. Fang, P. Xiu, Y. Li, R. Wen, and X. Liu, "Effect of spatial spectrum overlap on fourier ptychographic microscopy," *J. Innovative Opt. Health Sci.* **10**(02), 1641004 (2017).
27. K. Ramesh, *Developments in Photoelasticity*, 2053–2563 (IOP Publishing, 2021).
28. A. Asundi, "Phase shifting in photoelasticity," *Exp. Tech.* **17**(1), 19–23 (1993).
29. J. A. Quiroga and A. González-Cano, "Phase measuring algorithm for extraction of isochromatics of photoelastic fringe patterns," *Appl. Opt.* **36**(32), 8397–8402 (1997).
30. L.-H. Yeh, J. Dong, Z. Jingshan, L. Tian, M. Chen, G. Tang, M. Soltanolkotabi, and L. Waller, "Experimental robustness of fourier ptychography phase retrieval algorithms," *Opt. Express* **23**(26), 33214 (2015).
31. B. Xiao, H. Tang, Y. Jiang, W. Li, and G. Wang, "Brightness and contrast controllable image enhancement based on histogram specification," *Neurocomputing* **275**, 2798–2809 (2018).
32. X. Ou, G. Zheng, and C. Yang, "Embedded pupil function recovery for fourier ptychographic microscopy," *Opt. Express* **22**(5), 4960 (2014).
33. Y. Fan, J. Sun, Q. Chen, M. Wang, and C. Zuo, "Adaptive denoising method for fourier ptychographic microscopy," *Opt. Commun.* **404**, 23–31 (2017).
34. N. Hussain, M. Hasanzade, D. W. Breiby, and M. N. Akram, "Performance comparison of wavelet families for noise reduction and intensity thresholding in fourier ptychographic microscopy," *Opt. Commun.* **519**, 128400 (2022).